STRUCTURAL SCIENCE
CRYSTAL ENGINEERING
MATERIALS

ISSN: 2052-5206
journals.iucr.org/b

Multi-temperature study of potassium uridine-5′-monophosphate: electron density distribution and anharmonic motion modelling

Katarzyna N. Jarzembska, Katarzyna Ślepokura, Radosław Kamiński, Matthias J. Gutmann, Paulina M. Dominiak and Krzysztof Woźniak

Acta Cryst. (2017). B**73**, 550–564

STRUCTURAL SCIENCE
CRYSTAL ENGINEERING
MATERIALS

ISSN 2052-5206

Multi-temperature study of potassium uridine-5′-monophosphate: electron density distribution and anharmonic motion modelling

Katarzyna N. Jarzembska,[a]* Katarzyna Ślepokura,[b] Radosław Kamiński,[a] Matthias J. Gutmann,[c] Paulina M. Dominiak[d] and Krzysztof Woźniak[d]

[a]Department of Chemistry, University of Warsaw, Żwirki i Wigury 101, 02-089 Warsaw, Poland, [b]Department of Chemistry, University of Wrocław, Joliot-Curie 14, 50-383 Wrocław, Poland, [c]ISIS Neutron and Muon Source, Science and Technology Facilities Council, Rutherford Appleton Laboratory, Harwell Campus, Didcot, Oxfordshire OX11 0QX, England, and [d]Biological and Chemical Research Centre, Department of Chemistry, University of Warsaw, Żwirki i Wigury 101, 02-089 Warsaw, Poland. *Correspondence e-mail: katarzyna.jarzembska@gmail.com

Received 21 February 2017
Accepted 12 April 2017

Edited by C. Lecomte, Université de Lorraine, France

Keywords: nucleotides; uracil; charge density distribution; anharmonic motion; multi-temperature XRD.

CCDC references: 1533597; 1533598; 1533599; 1533600; 1533601

Supporting information: this article has supporting information at journals.iucr.org/b

Uridine, a nucleoside formed of a uracil fragment attached to a ribose ring *via* a β-N1-glycosidic bond, is one of the four basic components of ribonucleic acid. Here a new anhydrous structure and experimental charge density distribution analysis of a uridine-5′-monophosphate potassium salt, K(UMPH), is reported. The studied case constitutes the very first structure of a 5′-nucleotide potassium salt according to the Cambridge Structural Database. The excellent crystal quality allowed the collection of charge density data at various temperatures, *i.e.* 10, 100, 200 and 300 K on one single crystal. Crystal structure and charge density data were analysed thoroughly in the context of related literature-reported examples. Detailed analysis of the charge density distribution revealed elevated anharmonic motion of part of the uracil ring moiety relatively weakly interacting with the neighbouring species. The effect was manifested by alternate positive and negative residual density patterns observed for these atoms, which 'disappear' at low temperature. It also occurred that the potassium cation, quite uniformly coordinated by seven O atoms from all molecular fragments of the $UMPH^-$ anion, including the O atom from the ribofuranose ring, can be treated as spherical in the charge density model which was supported by theoretical calculations. Apart from the predominant electrostatic interactions, four relatively strong hydrogen bond types further support the stability of the crystal structure. This results in a compact and quite uniform structure (in all directions) of the studied crystal, as opposed to similar cases with layered architecture reported in the literature.

1. Introduction

Uridine is a nucleoside formed of a uracil fragment attached to a ribofuranose ring *via* a β-N1-glycosidic bond (Wu & Chargaff, 1969). Its phosphate constitutes one of the four basic components of ribonucleic acid (RNA) (Wan *et al.*, 2011), and among other roles plays an important part in the glycolysis pathway of galactose (Romano & Conway, 1996). In general, uridine phosphates, salts and all compounds containing nucleosides are of great interest in science. They are important molecules playing key roles in many biochemical processes, such as glucose metabolism, cell growth, gene transcription, K^+ and Na^+ ion transportation (Klohs *et al.*, 1984; Romano & Conway, 1996; Wan *et al.*, 2006; Desch *et al.*, 2010; Fajardo *et al.*, 2014). For instance, uridine monophosphate is used as a convenient delivery compound for uridine in brain research studies on Alzheimer's disease (Wurtman *et al.*, 2009). In view of the above, studies on their chemical nature, the ability to form hydrogen bonding and to interact with other molecules are crucial to understanding biochemical processes and to

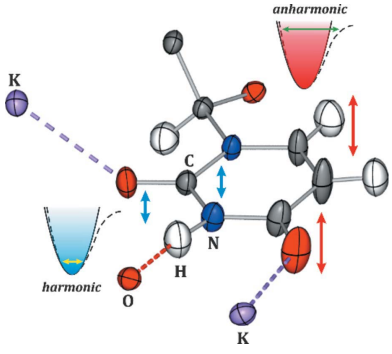

design new drugs, as well as give relevant insight into RNA and DNA structure and properties.

Nucleotides and their salts can also be very interesting as far as crystallography itself is concerned. In the Cambridge Structural Database (CSD; Groom *et al.*, 2016) more than 300 crystal structures containing the uridine fragment and its modifications have already been deposited. In the current contribution we focus our attention on the uridine-5′-monophosphate potassium salt, K(UMPH) (Scheme 1) and report its first anhydrous crystal structure. As the crystals were of superior quality, it was possible to conduct high-resolution X-ray diffraction experiments and thoroughly analyse charge density distribution and its subtle features in the selected single crystal at a number of temperatures, *i.e.* 10, 100, 200 and 300 K. Additionally, the experimental data were supplemented by a neutron diffraction data set collected at 10 K and subjected to computational analysis. The study constitutes somewhat a continuation of our previous structural and charge density investigations dedicated to nucleic acid base derivatives (Czyżnikowska *et al.*, 2010; Jarzembska *et al.*, 2012; Jarzembska, Goral *et al.*, 2013; Jarzembska, Kamiński *et al.*, 2013).

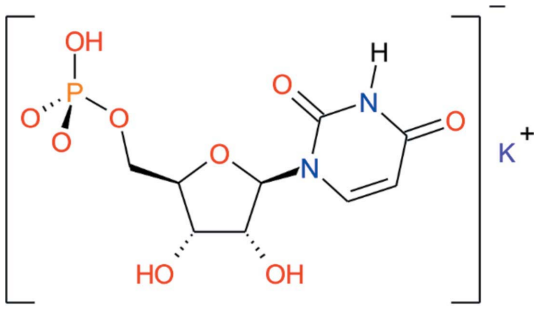

Scheme 1

2. Experimental

2.1. Materials

$UMPH_2$ was purchased from Sigma-Aldrich. K(UMPH) was obtained by reacting $UMPH_2$ with $KHCO_3$ in a 1-to-1 molar ratio. Both substrates were initially dissolved in water. In the next stage the majority of water was evaporated under dry nitrogen, and the final product was crystallized from the remaining solution with the addition of methanol. Such a procedure resulted in crystals of excellent quality which were subjected to further X-ray diffraction studies. We note that no single crystals were obtained from pure water.

2.2. Data collection and processing

A charge-density quality single crystal of a suitable size was chosen for the purpose of the current study, and thus multi-temperature, high-resolution data collections at 10, 100, 200 and 300 K were performed on one single crystal. Particular care was taken to record all low-angle reflections, which are crucial for a reliable charge density determination, and to minimize the number of reflections with $I/\sigma(I) < 3.0$ in the whole data set. It is worth mentioning that the collected reflection data were of high quality with well defined round reflections and the crystal exhibited very low mosaicity. The latter was indicated by the fact that two nearly *identical* data sets measured at 100 K, differing only in the single-frame scan width (0.50° *versus* 0.25°), gave results in favour of the thinner reflection slicing (R_{mrg} was half that for the 0.25° scan data set). This is in line with the previous literature studies on data quality with respect to the scan width (Sørensen & Larsen, 2003). Data processing and reduction was conducted using the native diffractometer software (Bruker AXS, 2015) and the *SORTAV* program (Blessing, 1987, 1995, 1997). All data sets exhibited a high-resolution limit of $(\sin\theta/\lambda)_{max} \simeq 1.2$ Å^{-1}, and overall completeness of more than 90%. Final data collection and reduction parameters are summarized in Table 1. Selected sets of raw diffraction frames and the associated data are accessible online under the following doi: http://doi.org/10.18150/repod.6850518 (Repository for Open Data, Interdisciplinary Centre for Mathematical and Computational Modelling, University of Warsaw, Warsaw, Poland). More information is available in the supporting information.

2.3. Structure solution and refinement.

In all cases the crystal structure was solved by a charge-flipping method (Oszlányi & Sütő, 2004, 2005; Palatinus, 2013) with the *SUPERFLIP* program (Palatinus & Chapuis, 2007). Initial independent atom model refinements were performed with the *JANA* program (Petříček *et al.*, 2014).

Multipole refinements for all data sets were carried out using the *MOPRO* suite (Guillot *et al.*, 2001; Jelsch *et al.*, 2005) combined with the current version of the University at Buffalo Data Bank (UBDB; Jarzembska & Dominiak, 2012), which employs the Hansen–Coppens multipole model (Hansen & Coppens, 1978). All the performed refinements were based on F, while only reflections fulfilling the $I \geq 3\sigma(I)$ criterion were taken into account. Such a cut-off does not influence the final model significantly, as has been shown recently (the results obtained with and without cut-off do not differ significantly considering the precision of the method; see also Fig. 2S in the supporting information; Kamiński *et al.*, 2014). In the refinement, the estimation of anisotropic H-atom atomic displacement parameters for all data sets was realised using the *SHADE* server (Madsen, 2006; Munshi *et al.*, 2008). It should be stressed that the *SHADE*-estimated values were also used in the case of the 10 K data, as not all H-atom atomic displacement parameters were of satisfactory quality (the time-of-flight neutron diffraction experiment was quite demanding due to the low scattering power of the sample and the complexity of the structure). In turn, the X—H bond lengths for the 10 K data set were restrained to neutron-derived distances with $\sigma = 0.001$. Similarly, for all other data sets, X—H bond lengths were restrained to neutron-normalized values with the same σ value. Even in the absence of the neutron data for higher temperatures, such an approach has been successfully applied in a variety of experimental charge density studies (Jelsch *et al.*, 2000; Chęcińska *et al.*, 2006; Meindl *et al.*, 2009; Jørgensen *et al.*, 2013; Jarzembska, Goral *et*

Table 1
Parameters characterizing the studied crystal, X-ray data collection and refinement.

For all structures: $C_9H_{12}KN_2O_9P$, M_r = 362.3, orthorhombic, $P2_12_12_1$, Z = 4, $F(000)$ = 744, colourless tablet of dimensions (mm) of 0.28 × 0.27 × 0.16. Experiments were carried out with Mo $K\alpha$ radiation using a CCD detector. Absorption was corrected for by multi-scan methods (Blessing, 1995). H atoms were treated by a mixture of independent and constrained refinement.

	10 K	100 K	200 K	300 K
Crystal data				
a, b, c (Å)	8.0778 (2),† 10.4023 (3), 16.0137 (4)†	8.0630 (3),† 10.4358 (5), 16.0092 (7)†	8.0670 (2), 10.4871 (3), 16.0561 (4)	8.0835 (2), 10.5221 (3), 16.0738 (4)
V (Å^3)	1345.59 (6)	1347.08 (10)	1358.34 (6)	1367.16 (6)
D_x (Mg m^{-3})	1.789	1.786	1.772	1.760
μ (mm^{-1})	0.57	0.56	0.56	0.56
Data collection				
T_{min}, T_{max}	0.808, 1.127	0.862, 0.890	0.860, 0.890	0.847, 0.929
R_{mrg} ‡	0.0408§	0.0255	0.0290	0.0292
No. of measured, independent and observed [$I \geq 3\sigma(I)$] reflections	80 683, 18 408, 17 834 (97%)¶	142 735, 18 693, 17 743 (95%)¶	97 227, 19 248, 15 846 (82%)¶	89 436, 18 254, 12 221 (67%)¶
θ values (°)	2.3–58.4	2.3–59.2	2.3–59.3	2.3–58.7
$(\sin\theta/\lambda)_{max}$ (Å^{-1})	1.20	1.21	1.21	1.21
Index ranges	$-18 \leq h \leq 18$, $-24 \leq k \leq 24$, $-38 \leq l \leq 37$	$-19 \leq h \leq 19$, $-23 \leq k \leq 23$, $-35 \leq l \leq 37$	$-18 \leq h \leq 19$, $-25 \leq k \leq 23$, $-38 \leq l \leq 21$	$-17 \leq h \leq 17$, $-24 \leq k \leq 12$, $-37 \leq l \leq 32$
Completeness (%)	95.0	93.8	95.6	91.8
Refinement				
No. of parameters, restraints	602, 12	642, 12	642, 12	642, 13
$R[F]$ [$I \geq 3\sigma(I)$], all data	0.0148, 0.0154	0.0111, 0.0124	0.0171, 0.0232	0.0194, 0.0336
$wR[F]$ [$I \geq 3\sigma(I)$], all data	0.0180, 0.0184	0.0141, 0.0145	0.0185, 0.0204	0.0222, 0.0263
$R[F^2]$ [$I \geq 3\sigma(I)$], all data	0.0241, 0.0241	0.0161, 0.0163	0.0289, 0.0298	0.0270, 0.0287
$S[F]$ [$I \geq 3\sigma(I)$], all data	0.836, 0.840	0.844, 0.848	0.893, 0.891	1.043, 1.005
$\Delta\rho_{res}^{min}$, $\Delta\rho_{res}^{max}$ (e Å^{-3}) [$I \geq 3\sigma(I)$]	−0.16, +0.15	−0.07, +0.06	−0.10, +0.11	−0.10, +0.09
$\Delta\rho_{res}^{min}$, $\Delta\rho_{res}^{max}$ (e Å^{-3}) (all data)	−0.16, +0.15	−0.08, +0.08	−0.13, +0.13	−0.11, +0.13
Additional comment	Harmonic model, X—H distances from neutron data	Anharmonic model	Anharmonic model	Anharmonic model, P_v (K1) = 6.30 (restrained)

† The larger values at 10 K when compared with those at 100 K may result from an anisotropic thermal response of the crystal to temperature changes, or from a different number of data used to refine the unit-cell parameters at both temperatures (note the unit-cell volume is smaller at 10 K than at 100 K). ‡ Definition of R_{mrg} is the same as in our previous papers Jarzembska, Kamiński *et al.* (2014) and Jarzembska *et al.* (2015), and follows definitions used by Blessing in the *SORTAV* program. § Note the larger R_{mrg} value relates to the lower redundancy of the data set. ¶ Numbers in parentheses constitute the percentage of the 'observed' unique reflections with respect to the total number of unique reflections.

al., 2013; Jarzembska, Hoser *et al.*, 2014). However, we note that the neutron-derived X—H bond lengths determined at 10 K were very close to the averaged values reported by Allen & Bruno (Allen *et al.*, 1987; Allen & Bruno, 2010). The multipole expansion was truncated at the hexadecapole (l_{max} = 4) and quadrupole (l_{max} = 2) levels for all non-H and H atoms, respectively. For more specific details see the supporting information (Su & Coppens, 1998; Macchi & Coppens, 2001; Volkov *et al.*, 2004; Hoser *et al.*, 2009; Zarychta *et al.*, 2011; Paul *et al.*, 2011; Jarzembska & Dominiak, 2012; Poulain-Paul *et al.*, 2012).

For the sake of further analysis it was particularly important to verify the approach to the refinement of the potassium ion. The refinement with standard atomic scattering factors (K^0: [core: $1s^22s^23s^22p^63p^6$, valence: $4s^1$] or [core: $1s^22s^23s^22p^6$, valence: $3p^64s^1$]) led to non-physical results (*e.g.* integrated AIM charges outside chemically sensible limits). In some of the published works (Koritsanszky *et al.*, 2000; Nelyubina *et al.*, 2009; Mermer & Starynowicz, 2012) the P_v parameter was constrained to a specified value. In our case, an acceptable model was obtained with the ionic scattering factor having $3p$ electrons moved to the valence shell (K^+: [core: $1s^22s^23s^22p^6$, valence: $3p^6$]). On the other hand, there still remains the question of whether the the K atom is spherical or not. When compared with much more rigid Li or Na cations, it possesses more electrons and is generally known as being more polarisable (Molof *et al.*, 1974; Ekstrom *et al.*, 1995; Holmgren *et al.*, 2010). To the best of our knowledge, in the available literature potassium was most often considered as being spherical (Koritsanszky *et al.*, 2000; Nelyubina *et al.*, 2009; Mermer & Starynowicz, 2012). Nevertheless, in the advent of crystallography and experimental methods which allow the collection of high-quality data, it is tempting to extract and model on such heavy atoms any aspherical deformations present. This is especially interesting considering the latest reports on core deformation effects suggested on the basis of experimental charge density data (Fischer *et al.*, 2011; Zhurov & Pinkerton, 2013; Bindzus *et al.*, 2014). Therefore, both possibilities were investigated, *i.e.* treating potassium as spherical (with only the P_v parameter refined) or aspherical (with multipole expansion applied to the hexadecapole level). Obviously, the aspherical model gave a slightly better fit, reflected in lower R-factors and

residual density values (for numerical details see the supporting information). This is due to the larger number of refined parameters. Nevertheless, the differences are negligible, as both models yielded very similar integrated AIM charges for potassium (*e.g.* for the 10 K data set: +0.70 e and +0.68 e for the spherical and aspherical models, respectively). In order to decide which model is more physically sound we compared electron distribution on the potassium centre in both models (for 10 K data set), spherical (Fig. 1*a*) and aspherical (Fig. 1*b*), with that obtained by theoretical periodic computations (Fig. 1*c*). The latter, theoretical results, further described in detail, are treated here as an independent reference. The theory-computed negative Laplacian map clearly shows the absence of noticeable valence-shell charge concentrations in the potassium outer shell. Such a theoretical outcome best supports the spherical multipole model for the potassium ion. In the case of the 100 K data set the effect is similar, but less pronounced. Consequently, in all models derived for the purpose of this study the spherical description of the potassium ion was applied. We note here that to make the 300 K charge density model reasonable, the P_v parameter for the potassium centre was restrained to the value of 6.3 e with $\sigma = 0.01$ (based on the results from the lower-temperature data sets). For more details see also the supporting information (Moss *et al.*, 1995; Souhassou *et al.*, 1995; Espinosa *et al.*, 1996; Yufit *et al.*, 2000; Janicki & Starynowicz, 2010; Mermer & Starynowicz, 2011, 2012; Mermer *et al.*, 2015; Kinzhybalo *et al.*, 2013; Starynowicz & Lis, 2014; Volkov *et al.*, 2016).

Despite the very low residual density extreme values obtained for models at all temperatures and satisfactory *R*-factors (considering non-trivial description of the potassium and phosphorus atoms), careful inspection of the residual density for 100, 200 and 300 K data sets revealed some systematic effects within the uracil fragment. Although the details are described in the following section of this paper, we note here that we were able to take these effects into account by refining the third-order Gram–Charlier parameters (Johnson, 1969; Kuhs, 1983; Scheringer, 1985). The physical reliability of the anharmonic model was confirmed by the probability density function (PDF) computed with the *JANA* program. Furthermore, the absence of these effects in the 10 K data set (anharmonic effects for non-H atoms are expected to diminish significantly with temperature lowering) additionally supports such data treatment. The refined anharmonic parameters appeared to be rather weakly correlated with multipolar parameters. All these results are in line with many recent literature reports on this matter (Scheins *et al.*, 2010; Zhurov *et al.*, 2011; Herbst-Irmer *et al.*, 2013; Poulain *et al.*, 2014), where high-quality data allow for reliable deconvolution of electron density and thermal motion features. More details can be found in the supporting information.

In general, determination of absolute structure was not needed due to the known configuration of the studied compound (β-D-ribofuranose ring). However, as a test, the Flack parameter was determined in each case (Spek, 2015; Hooft *et al.*, 2008) and its value was very close to zero (see also the supporting information). Residual density properties were evaluated with the *JNK2RDA* program (Meindl & Henn, 2008). The analysis shows that the refinement resulted in models characterized by the flat and almost featureless residual density distribution. All the final refinement statistics are summarized in Table 1. The respective CIF files are given in the supporting information, or can be retrieved from the Cambridge Structural Database (CSD) (Groom *et al.*, 2016). For more information also see the supporting information (Hirshfeld, 1976; Kuhs, 1988, 1992; Niepötter *et al.*, 2015).

2.4. Periodic computations

Theoretical charge density distribution was evaluated on the basis of wavefunctions calculated using the *CRYSTAL* program package (Dovesi *et al.*, 2005, 2009) (*CRYSTAL09* edition) at the DFT(B3LYP) level of theory (Perdew, 1986; Becke, 1988; Lee *et al.*, 1988). The POB-TZVP molecular all-electron basis set (Peintinger *et al.*, 2013) dedicated to solid state systems was applied for the purpose of the conducted

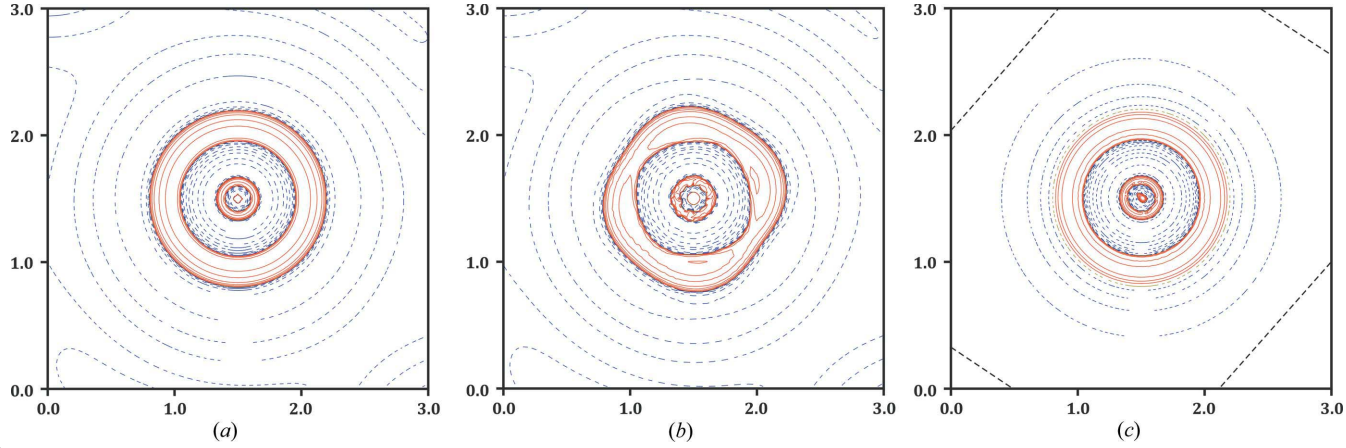

Figure 1
Electron density Laplacian maps in the vicinity of the potassium ion for multipole models with spherically (*a*) and aspherically (*b*) refined potassium fragment, and resulting from theoretical periodic computations (*c*) (logarithmic contours; blue dashed lines – positive values, red solid lines – negative values; K1—O4—O2 plane). Experimental maps were computed for the 10 K data set (the respective figures for the 100 K data set are available from the supporting information).

computations. The evaluation of Coulomb and exchange series was controlled by five thresholds, set arbitrarily to the values of 10^{-7}, 10^{-7}, 10^{-7}, 10^{-7} and 10^{-25}, whereas the shrinking factor was equal to 8. *CRYSTAL* program input files were prepared with the *CLUSTERGEN* program (Kamiński *et al.*, 2013).

2.5. Evaluation of the charge density distribution properties

The experimental charge density distribution obtained with the multipolar approach was analysed by means of Bader's quantum theory of atoms in molecules (QTAIM; Bader, 1994). The *VMOPRO* module (part of the *MOPRO* package) was used for Fourier syntheses and bond critical point evaluation. Visualization of bond paths was accomplished with the *MOPROVIEWER* program (Guillot, 2012). Evaluation and integration of atomic basins were performed with the *XD* (Volkov *et al.*, 2016) and *TOPOND* (Gatti *et al.*, 1994; Bertini *et al.*, 2007) programs for experimental and theoretical data, respectively.

2.6. Neutron diffraction

A single-crystal time-of-flight neutron diffraction experiment was performed at the SXD beamline (Keen *et al.*, 2006), at the neutron spallation source at the ISIS facility (Oxfordshire, UK). For the purpose of the experiment a single crystal of size approximately equal to 1 mm × 1 mm × 2 mm was attached to an Al pin with adhesive Al tape, and cooled to 10 K in a closed-cycle refrigerator with He as an exchange gas. Eleven crystal orientations were recorded in total, each exposed for 8–16 h. We note that the last three orientations were collected simultaneously for three crystals of the same size (Wilson, 1997). Data reduction was accomplished using the locally available *SXD2001* program (Keen *et al.*, 2006). The crystal structure (with anisotropic H-atom displacement parameters) was then refined in the *JANA* package directly from the time-of-flight data. It is also worth noting that the extinction was successfully modelled using the Becker–Coppens approach (Becker & Coppens, 1974*a*,*b*, 1975). More information and the CIF file are available in the supporting information. Raw neutron diffraction frames and the associated data are accessible online under the following doi: http://doi.org/10.18150/repod.6850518 (Repository for Open Data).

3. Results and discussion

3.1. General remarks

As already mentioned, up to now, more than 300 crystal structures containing the uridine fragment and its substituted derivatives are present in the CSD. Out of that number, 268 entries contain atomic coordinates. Concerning solely uridine-like phosphates, one can find barium uridine-5′-monophosphate [Ba(UMP)] monohydrate (refcode: BAURIP; Shefter & Trueblood, 1965), potassium dihydrouridine-3′-monophosphate hemihydrate (refcode: KURDMP; Emerson & Sundaralingam, 1980), dipotassium uridine-5′-diphosphate trihydrate (refcode: KURDPI; Viswamitra *et al.*, 1979), disodium deoxyuridine-5′-monophosphate pentahydrate (refcode: NADOUR; Viswamitra *et al.*, 1980), disodium uridine-3′-monophosphate tetrahydrate (refcode: SURIDP; Viswamitra *et al.*, 1972), disodium uridine-5′-monophosphate [Na_2(UMP)] heptahydrate (refcode: SURIPH10; Seshadri *et al.*, 1980), and uridine-3′-monophosphate monohydrate (refcode: URIDMP10; Srikrishnan *et al.*, 1979). Clearly, all the crystal structures are hydrates and only two contain the uridine-5′-monophosphate (UMP) moiety (refcodes: BAURIP and SURIPH10). However, in none of them is the protonation state of the UMP fragment the same as that found in K(UMPH). Furthermore, potassium ions are present in only two other structures from the depicted group (refcodes: KURDMP and KURDPI). Consequently, the reported K(UMPH) salt (Scheme 1) constitutes the first anhydrous solid-state form of the single-deprotonated uridine-5′-monophosphate anion ($UMPH^-$). The common feature of these salts is that they are all chiral and crystallize in chiral space groups. Nevertheless, they differ in the packing preferences. Interestingly, the topology of the Na_2(UMP) heptahydrate crystal structure (refcode: SURIPH10) reported in the literature, as well as that of the related barium salt (refcode: BAURIP), somewhat resembles the topology of aromatic fluoroborate potassium salts, which form layered architectures in the solid state (Conole *et al.*, 1995; Harrison & Wardell, 2014; Kamiński *et al.*, 2016). These two structures are very similar to each other, except for some differences induced by larger barium species (see the supporting information) when compared with sodium cations (note that Na^+ ions were not included in the refined model at that time; Seshadri *et al.*, 1980). In both structures layers formed by metal centres coordinated by water molecules may be distinguished. Such layers are separated by the UMP^{2-} anions, which act as molecular linkers, further coordinating metal cations on one side with the phosphate group and one uracil oxygen, while on the opposite side by the remaining uracil oxygen and the ribofuranose ring hydroxyl groups. In this respect the overall architecture of the new K(UMPH) structure (Fig. 2) differs from the two described cases due to the absence of water

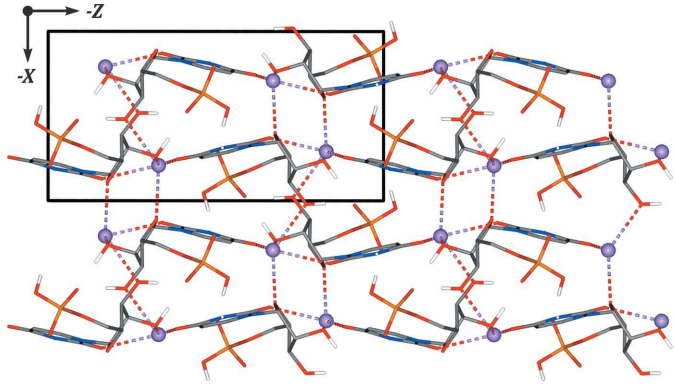

Figure 2
Packing of K(UMPH) molecules in the crystal lattice; potassium ions represented by spheres.

Table 2
Selected Bader charges (Q_{AIM}) and atomic basin volumes (V_{AIM}) for the K(UMPH) species present in the crystal lattice.

Data given for the 10 K data set and for *TOPOND* results; for more data see the supporting information. The respective literature data for uracil-core-based fragments are also included.

	10 K data		Theory		1mT$_c$†	6m2tu‡
Atom	Q_{AIM} (e)	V_{AIM} (Å^3)	Q_{AIM} (e)	V_{AIM} (Å^3)	Q_{AIM} (e)	Q_{AIM} (e)
K1	+0.70	21.53	+0.92	20.43	–	–
P1	+2.91	6.81	+3.77	3.25	–	–
O1	−1.16	13.71	−1.30	14.37	–	–
O2	−1.32	17.55	−1.52	18.76	–	–
O3	−1.29	17.48	−1.53	18.77	–	–
O4	−1.29	17.44	−1.45	18.39	–	–
O8	−1.07	19.25	−1.15	20.13	−1.24	−0.27§
O9	−1.09	19.65	−1.16	20.57	−1.24	−1.16
N1	−0.98	11.33	−1.06	11.39	−0.73	−1.00
N2	−1.02	15.02	−1.10	15.5	−1.10	−1.06
C6	+1.60	5.26	+1.64	5.16	+1.66	+0.56
C7	+1.37	7.02	+1.23	6.90	+1.37	+1.33
C8	+0.19	11.97	+0.03	12.56	−0.32	+0.03
C9	+0.08	12.83	+0.36	10.84	+0.38	+0.23
H8	+0.16	5.81	+0.08	6.56	–	+0.12
H9	+0.19	5.24	+0.15	5.68	+0.17	–
H10	+0.49	2.54	+0.52	2.38	+0.46	+0.42

† Data taken from literature for 1-methylthymine (Jarzembska, Goral *et al.*, 2013). ‡ Data taken from literature for 6-methyl-2-thiouracil (Jarzembska, Kamiński *et al.*, 2013). § Sulfur atom.

Table 3
Selected QTAIM parameters at BCPs for strong interactions in the K(UMPH) species in the crystal lattice.

d is distance between bonded atoms, d_1 and d_2 are distances from first and second atom to the bond critical point, respectively; ρ is the electron density; ε is the bond ellipticity. The given results apply to the 10 K data set (for more data see the supporting information).

Bond	d (Å)	d_1 (Å)	d_2 (Å)	$\rho(\mathbf{r}_{BCP})$ (e Å^{-3})	$\nabla^2\rho(\mathbf{r}_{BCP})$ (e Å^{-5})	ε
K1···O2	2.9008 (2)	1.484	1.420	0.1	1.3	0.01
K1···O4	2.9253 (3)	1.499	1.430	0.1	1.2	0.03
K1···O5^{i}	2.7261 (2)	1.418	1.308	0.1	1.9	0.02
K1···O8^{ii}	2.8008 (2)	1.454	1.347	0.1	1.6	0.00
K1···O9^{iii}	2.7278 (3)	1.413	1.315	0.1	1.9	0.01
K1···O7^{iv}	2.8040 (2)	1.445	1.360	0.1	1.6	0.04
K1···O6^{v}	2.7480 (2)	1.420	1.328	0.1	1.9	0.02
P1—O1	1.6017 (2)	0.672	0.934	1.2	8.1	0.16
P1—O2	1.5132 (2)	0.636	0.878	1.4	19.5	0.16
P1—O3	1.4970 (2)	0.625	0.874	1.4	23.5	0.10
P1—O4	1.5575 (2)	0.652	0.908	1.2	13.9	0.27
N1—C6	1.3847 (3)	0.801	0.584	2.3	−22.6	0.21
C6—N2	1.3716 (3)	0.774	0.598	2.3	−23.4	0.17
N2—C7	1.3903 (3)	0.850	0.540	2.0	−21.1	0.23
C7—C8	1.4437 (3)	0.792	0.652	2.1	−19.2	0.31
C8—C9	1.3521 (3)	0.746	0.606	2.3	−22.6	0.27
C9—N1	1.3735 (3)	0.818	0.556	2.1	−20.5	0.17
C6—O8	1.2272 (3)	0.796	0.432	3.0	−33.6	0.06
C7—O9	1.2358 (3)	0.815	0.422	2.7	−23.7	0.04
C8—H8	1.0711 (8)	0.660	0.411	1.9	−24.7	0.15
C9—H9	1.0730 (8)	0.721	0.353	2.0	−24.7	0.00
N2—H10	1.0410 (8)	0.775	0.266	2.1	−30.0	0.07

Symmetry codes: (i) $x-\frac{1}{2}, -y+\frac{1}{2}, -z+1$; (ii) $-x+\frac{1}{2}, -y, +z+\frac{1}{2}$; (iii) $-x+\frac{1}{2}, -y, +z+\frac{1}{2}$; (iv) $-x+\frac{1}{2}, -y, +z+\frac{1}{2}$; (v) $x+\frac{1}{2}, -y+\frac{1}{2}, -z+1$.

molecules and different protonation state of the anion. Thus, apart from the above-mentioned O atoms engaged in the metal centre coordination, the O5 atom from the sugar ring (Fig. 3) saturates the potassium coordination sphere instead of the water species. This, among others factors, imposes a different arrangement of potassium cations around the UMPH$^-$ fragments, and also a different conformation of the ribofuranose ring, resulting in a more uniform crystal packing in all directions, with no disorder. All that may in turn contribute to the observed distinctive quality of K(UMPH) crystals.

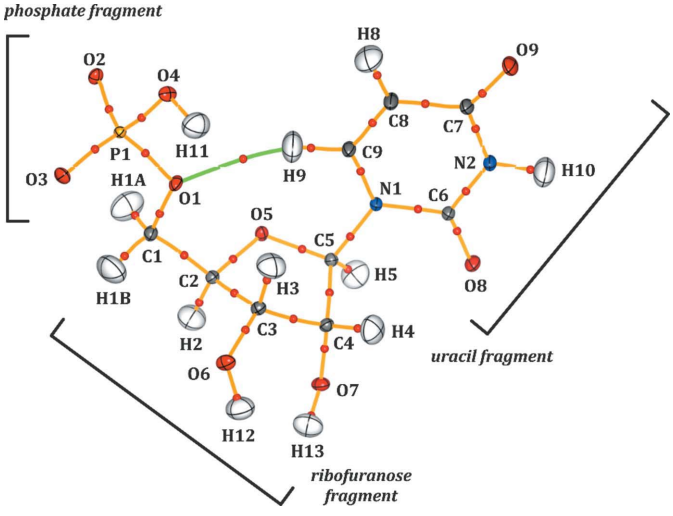

Figure 3
Molecular graph for the 10 K data set showing bond paths (yellow solid lines) and bond critical points (small red spheres) for the UMPH$^-$ anion. Labelling and estimation of atomic thermal motion as atomic displacement parameters is included (the absent potassium cation is labelled K1; ellipsoids are drawn at the 70% probability level). The bond path derived for the weak intramolecular H9···O1 interaction is coloured green. Structural fragments (uracil, ribofuranose and phosphate) are additionally depicted.

Finally, it is worth noting that the reported crystal structure is the first example of the 5′-nucleotide (*i.e.* 5′-nucleoside monophosphate) potassium salt structure ever deposited in the CSD. Considering the two mentioned potassium-containing structures related to K(UMPH), the potassium dihydrouridine-3′-monophosphate hemihydrate (refcode: KURDMP) forms layers, whereas the dipotassium uridine-5′-diphosphate trihydrate (refcode: KURDPI) does not. However, in both structures potassium cations are coordinated by O atoms from all molecular units, including water species, thus potassium achieves a coordination number of 7. Similarly, in the analysed K(UMPH) structure the potassium cation is coordinated by seven O atoms, which will be discussed in detail in the following section in the context of electronic properties.

3.2. Topological analysis of charge density distribution

The full multipole refinements yielded a set of crystal structures and the charge density models were determined at all four temperatures: 10, 100, 200 and 300 K, showing how the

Table 4
Selected QTAIM parameters for weak intermolecular interactions at the positions of the respective BCPs in the K(UMPH) crystal.

E_{EL} is the interaction energy calculated based on the Espinosa–Lecomte approximation. The given results apply to the 10 and 100 K data sets (for more data see supporting information).

Interaction	d (Å)	d_1 (Å)	d_2 (Å)	$\rho(\mathbf{r}_{BCP})$ (e Å^{-3})	$\nabla^2\rho(\mathbf{r}_{BCP})$ (e Å^{-5})	E_{EL} (kJ mol^{-1})	Remarks
10 K data set							
O2···H11^{i}	1.542 (1)	1.037	0.506	0.53	1.03	−113	O4—H11···O2†
O3···H13^{ii}	1.669 (2)	1.137	0.532	0.26	3.76	−51	O7—H13···O3‡
O2···H10^{iii}	1.724 (2)	1.146	0.579	0.26	3.41	−49	N2—H10···O2
O3···H12^{ii}	1.755 (2)	1.149	0.607	0.30	1.18	−48	O6—H12···O3‡
O1···H9	2.396 (5)	1.418	0.983	0.08	0.75	−8	C9—H9···O1§
O6···H4^{ii}	2.656 (5)	1.476	1.192	0.06	0.54	−5	C4—H4···O6
O8···H2^{iv}	2.736 (7)	1.564	1.232	0.03	0.37	−3	C2—H2···O8
O7···H8^{v}	2.766 (5)	1.624	1.172	0.03	0.28	−2	C8—H8···O7
O6···H1B^{vi}	3.050 (5)	1.717	1.393	0.03	0.26	−2	C1—H1*B*···O6
O9···H1B^{vii}	2.876 (7)	1.653	1.308	0.02	0.27	−2	C1—H1*B*···O9
O9···H3^{viii}	3.127 (9)	1.726	1.407	0.02	0.25	−2	C3—H3···O9
100 K data set							
O2···H11^{i}	1.541 (1)	1.042	0.496	0.54	0.03	−114	O4—H11···O2†
O3···H13^{ii}	1.685 (2)	1.133	0.550	0.30	2.59	−53	O7—H13···O3‡
O2···H10^{iii}	1.744 (3)	1.150	0.589	0.30	1.43	−48	N2—H10···O2
O3···H12^{ii}	1.758 (1)	1.174	0.579	0.23	2.65	−40	O6—H12···O3§
O1···H9	2.394 (5)	1.473	0.961	0.05	0.81	−6	C9—H9···O1§
O6···H4^{ii}	2.656 (5)	1.490	1.191	0.05	0.49	−5	C4—H4···O6
O8···H2^{iv}	2.730 (8)	1.570	1.216	0.03	0.39	−3	C2—H2···O8
O7···H8^{v}	2.773 (5)	1.710	1.163	0.02	0.37	−2	C8—H8···O7
O6···H1*B*^{vi}	3.068 (5)	1.747	1.385	0.03	0.26	−2	C1—H1*B*···O6
O9···H1*B*^{vii}	2.880 (7)	1.637	1.299	0.02	0.30	−2	C1—H1*B*···O9
O9···H3^{viii}	3.119 (9)	1.722	1.355	0.02	0.25	−2	C3—H3···O9

Symmetry codes: (i) $x+\frac{1}{2}, -y+\frac{1}{2}, -z+1$; (ii) $-x, y+\frac{1}{2}, -z+\frac{1}{2}$; (iii) $x, y+1, z$; (iv) $-x+1, y-\frac{1}{2}, -z+\frac{1}{2}$; (v) $-x+\frac{1}{2}, -y, z-\frac{1}{2}$; (vi) $-x, y-\frac{1}{2}, -z+\frac{1}{2}$; (vii) $-x+\frac{1}{2}, -y, z+\frac{1}{2}$; (viii) $x+\frac{1}{2}, -y-\frac{1}{2}, -z+1$. † Interaction between two phosphate groups. ‡ Interaction in 'triangle' pattern with hydroxyl groups from ribofuranose ring. § Intramolecular interaction (depicted in green in Fig. 3).

static electron density distribution evolves with temperature. Despite the higher R_{mrg} factor (see the respective comment in Table 1), the main part of the following analysis will be based on the 10 K data set, as at this very low temperature the electron density and thermal motion features can be deconvoluted most reliably. The molecular graph with the associated ellipsoid representation of atomic displacement parameters is presented in Fig. 3, whereas the numerical parameters characterizing the structure are summarized in Tables 2–4.

At the start of the charge density distribution analysis, it is worth discussing the potassium ion and its coordination sphere in the studied structure. As already mentioned, the potassium cation is seven-coordinated (Fig. 4) and is bound by almost all the available O atoms of the counterion, except for O1 and O3. These two remaining O atoms are involved either in the intermolecular O—H···O hydrogen bonds (O6—H12···O3 and O7—H13···O3; Table 4), or in the weak intramolecular interaction C9—H9···O1 (depicted in green in Fig. 3). The bond critical point (BCP) properties for K···O interactions compare well with those reported in the literature (Table 3). The electron density at the BCPs is close to 0.1 e Å^{-3}, whereas the Laplacian is only slightly positive (in our case it does not exceed 2.0 e Å^{-5}). These features indicate the closed-shell character of such interactions, which is illustrated well by the Laplacian map in the vicinity of the potassium centre (Fig. 4*b*). The above conclusions apply to all temperatures (see the supporting information). Finally, it should be noted that the spherical multipole model relevance for the potassium centre may result from its charge and the rather uniform distribution of O atoms in its coordination sphere.

Apart from the already mentioned strong electrostatic interactions between K and O atoms, the studied crystal structure is stabilized by numerous hydrogen bonds and weaker intermolecular contacts (Table 4). Analysis of hydrogen bonds' topological parameters reveals several interesting facts. Firstly, the hydrogen bond formed between two phosphate groups, namely O4—H11···O2, appears to be very strong. Electron density in the respective BCP, as for a hydrogen bond, is relatively high and exceeds the value of 0.5 e Å^{-3}. According to the Espinosa–Lecomte estimation of the interaction energy (Espinosa *et al.*, 1998,

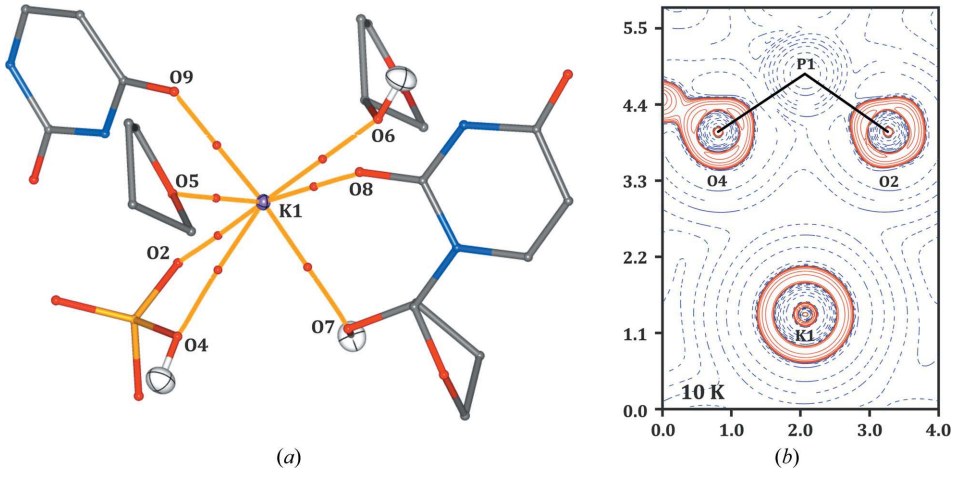

Figure 4
(*a*) Bond paths and bond critical points in the potassium coordination sphere (symmetry codes are omitted for clarity). (*b*) Exemplary Laplacian map in the vicinity of the potassium ion (logarithmic contours; blue dashed lines – positive values, red solid lines – negative values; note that the P1 atom is out of plane). Both figures made for the 10 K data set.

1999), the energy of this interaction reaches almost −115 kJ mol^{-1}. The obtained parameters resemble that characterizing very strong hydrogen bonds reported in the literature (Grabowski, 2001; Dominiak *et al.*, 2006; Hoser *et al.*, 2010; Kamiński *et al.*, 2014). On the other hand, it should be noted here that both phosphate groups bear the charge of −1.53 e, so the described hydrogen bond just somewhat diminishes the strong repulsive interaction between these two negatively charged species. A different situation is observed for the remaining hydrogen bonds encountered in the studied structure, *i.e.* N1—H10···O2, O6—H12···O3 and O7—H13···O3, which are considerably weaker (interaction energy oscillates around −50 kJ mol^{-1} at 10 K), however, the interacting species do not repel each other. The first one is the interaction between the N—H species from the almost neutral uracil fragment (−0.10 e) and the negatively charged phosphate group, whereas the two others form a 'triangle' pattern involving two hydroxyl groups from the positively charged ribofuranose moiety (+0.93 e) pointing towards the O3 atom from the phosphate group (Fig. 5). Thus, the last two interactions are even strengthened by the electrostatic attraction between the moieties engaged in the respective hydrogen bonds, whereas the phosphate group acts in the crystal structure both as a hydrogen bond donor and acceptor. It is worth noting that the hydrogen bonds' geometrical parameters, as well as topological and energetic features, do not change much with temperature (within the estimated method precision; Kamiński *et al.*, 2014). This confirms the rigidity of the structure, and is also reflected in the minor influence of temperature on the unit-cell parameters, both typical for ionic crystals (please note the unit cell derived from the neutron diffraction data somewhat deviates from that obtained using the X-ray data set at 10 K, which may be attributed to the fewer data points used to refine the unit-cell parameters for the TOF data and different experimental conditions, *e.g.* quite large detector pixels). Nevertheless, the overall electron density in the vicinity of H atoms visibly varies with temperature. In the case of the N—H···O interaction, the 100 K model yielded a polarized H10 atom, but the 10 K model did not. The opposite situation was observed for the H12 atom, being polarized at 10 K, but not at 100 K. Thus, the polarization features of the H atoms involved in strong hydrogen bonds seem to be related to the actual structure at a given temperature. Interestingly, at higher temperatures (200 and 300 K) neither of these atoms is polarized. Such an outcome, however, may be considered to be a drawback of the mentioned incomplete deconvolution of thermal motion and static charge density in the corresponding models (see comment later in the text). Similar polarization effects have been reported previously (Overgaard *et al.*, 2001; Roversi & Destro, 2004; Śledź *et al.*, 2010; Jarzembska, Kamiński *et al.*, 2014), and the discussion whether they result only from the refinement of quadrupoles for H atoms, or describe some physical phenomena, is still open. It should be noted here that to date no such polarization effects were indicated by theoretical computations. Thus, to answer this question more studies are necessary, preferably some solid comparison of various electron density models, including

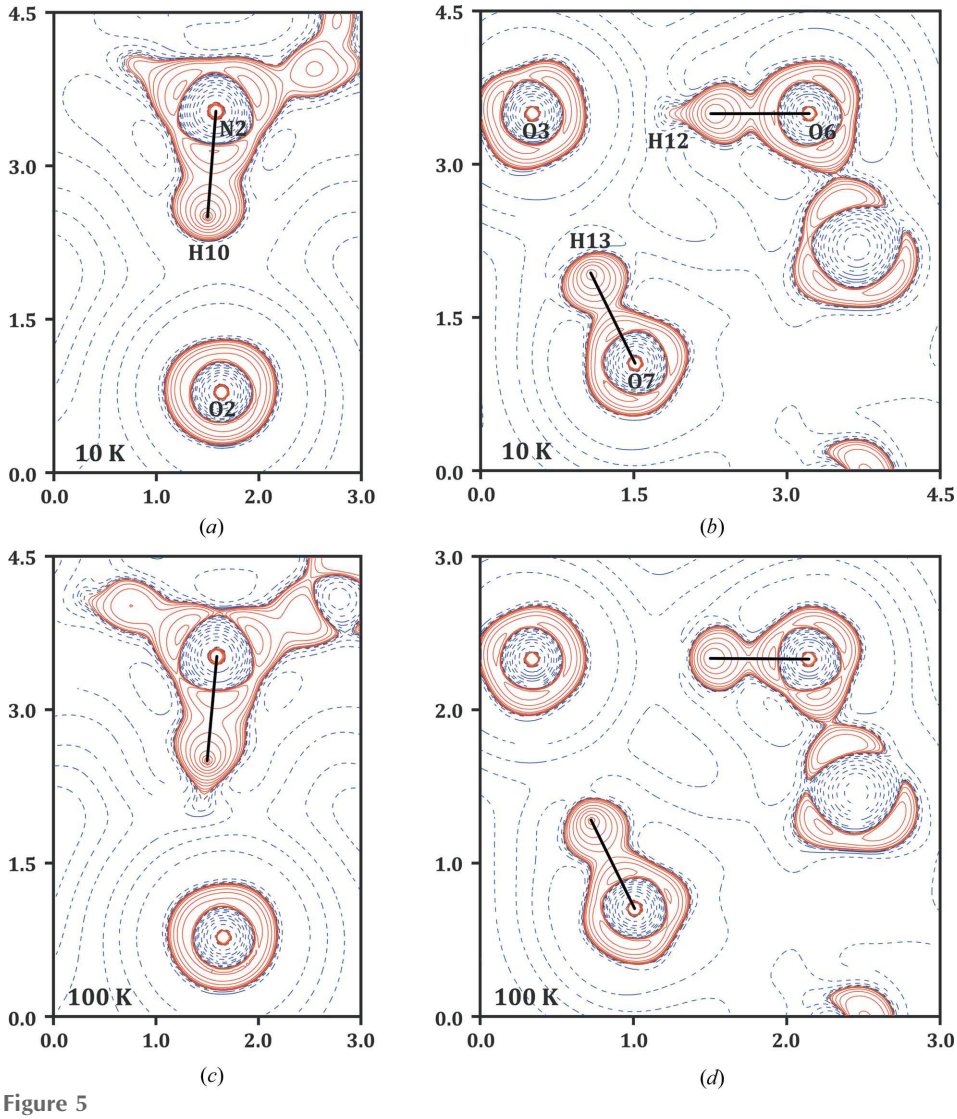

Figure 5
Laplacian maps for selected hydrogen bonds (logarithmic contours; blue dashed lines – positive values, red solid lines – negative values). Atom labelling is shown in (*a*) and (*b*), and applies for (*c*) and (*d*), respectively.

wavefunction-based approaches to experimental charge density modelling (Massa *et al.*, 1985; Howard *et al.*, 1994; Jayatilaka & Grimwood, 2001; Hibbs *et al.*, 2005; Dos Santos *et al.*, 2014).

Electron density distribution on the uracil moiety at various temperatures constitutes another important issue. Deformation density and Laplacian maps are presented in Figs. 6 and 7, respectively. It is clearly visible that the data for 10 and 100 K are of high quality. In the case of the 200 K data set, some spurious features start to appear near the H-atom positions. Consequently, for the 300 K data such effects are even more pronounced. In addition, in the latter case the O9 atom electron lone pairs seem to be incorrectly described. Also, the C6—O8 bond path deviates significantly from the ring plane (the Laplacian distribution appears to be discontinuous along this bond in the projection in Fig. 7*d*). This is probably due to the earlier-mentioned incomplete deconvolution of electron density and thermal motion features at higher temperatures. However, in general, such effects can also have other origins, among which is the thermal diffuse scattering (TDS) being most significant at high angles and at elevated temperatures. Nevertheless, during the model evaluation the TDS was either rather small, or could not be decoupled easily from other resolution-dependent issues, such as possible scaling procedure deficiencies (see the supporting information for more details). Interestingly, the refinement of the 300 K data with the O9 atom multipolar parameters fixed at the UBDB values results in a more reasonable deformation density for this atom with almost no harm to the model quality indicators, as *e.g.* *R*-factors, extreme residual density values, *etc.* Furthermore, the overall shape of the deformation density derived for the O9 atom (*i.e.* the difference between the two referred models) visualized by the three-dimensional plot cannot be explained either by changes in the intermolecular interactions or by anharmonic motion, as discussed further in the text (see Fig. 5S). As explained previously, the pattern of intermolecular interactions does not change much with temperature, thus the expected shape of the O9 atom should not change much either. Based on that, it can be concluded that due to the accumulation of various errors (such as TDS), the 300 K data suffers from some incomplete deconvolution of electron density and thermal motion. The incomplete deconvolution issue has also been discussed by Zhurov *et al.* (2011), who analysed the anharmonic motion effects. On the other hand, Zhurov *et al.* refined *all* non-H atoms anharmonically, which considerably increases the number of used parameters. For the purpose of the current study this approach was not applied due to the size of the molecule and the complexity of the whole structure. The anharmonic motion of the *selected* atoms is discussed in detail further in the text.

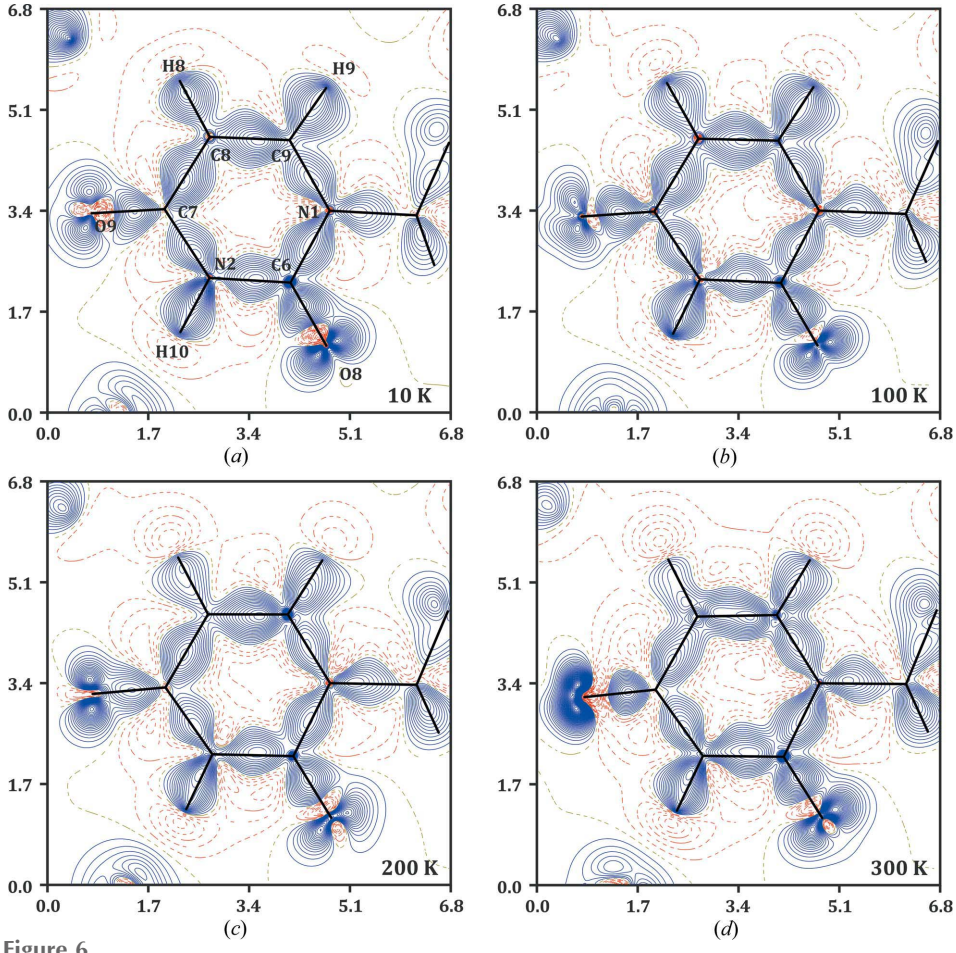

Figure 6
Deformation density maps for the uracil fragment (contouring at 0.05 e Å^{-3}; blue dashed lines – positive values, red solid lines – negative values). The common atom labelling is shown only in (*a*).

At this point, it is worthwhile discussing the results of the topological analysis with regard to our previous experimental charge density studies of uracil-core-based systems, namely the 6-methyl-2-thiouracil (6m2tU) (Jarzembska, Kamiński *et al.*, 2013) and 1-methylthymine(1mT$_c$)(Jarzembska, Goral *et al.*, 2013). Direct comparison of BCP properties indicates that all such fragments are rather similar (obviously except for the C—O bond *versus* C—S bond in 6m2tU). Nevertheless, a comparison of the charges of atoms common for all structures can be more informative (Table 2). It may be noticed that in 1mTc almost all atoms tend to have roughly similar charges to those obtained for the studied uracil moiety, yet they are noticeably different (taking into account the precision of the method at the suggested 0.1 e level; Kamiński *et al.*, 2014). The largest difference is observed for the C8

atom, due to its different local environment. However, some other more pronounced discrepancies are found for the N1 and C9 atoms (the differences reach 0.25 e and 0.30 e, respectively), despite their close similarity in both structures. 6m2tU differs from the studied fragment to a similar extent as $1mT_c$. In spite of the obvious differences between the S *versus* O atoms (+0.80 e difference) and their close neighbour, *i.e.* the C6 atom, some relatively significant discrepancies are also observed for the C8 and C9 atoms (around 0.15–0.16 e difference). The former atom is connected to the methyl group, and thus has a different local environment than that in the K(UMPH) structure. In the literature one can also find charge density results for 2-thiouracil and cytosine published by Munshi & Row (2006), but no direct comparison was possible because no integrated charges had been reported.

Table 5
Two largest anharmonic parameters (C_{111} and C_{112}) for C7, C8, C9 and O9 atoms.

Parameter (atom)	100 K	200 K	300 K
C_{111}, C_{112} (C7)	0.0034 (1), −0.0019 (2)	0.0083 (5), −0.0056 (7)	0.0146 (13, −0.0102 (16)
C_{111}, C_{112} (C8)	0.0016 (1), −0.0011 (1)	0.0041 (3), −0.0029 (3)	0.0058 (6), −0.0051 (5)
C_{111}, C_{112} (C9)	0.0013 (1), −0.0010 (1)	0.0046 (3), −0.0036 (3)	0.0070 (6), −0.0066 (5)
C_{111}, C_{112} (O9)	0.0040 (1), −0.0024 (1)	0.0114 (5), −0.0092 (5)	0.0193 (13), −0.0174 (9)

3.3. Anharmonic motion

Finally, it is worth analysing the refined anharmonic motion parameters for all models. The anharmonicity is most clearly visible at high-resolution residual density maps ($\sin\theta/\lambda \geq 0.8$ Å^{-1}), even though the first sign of its presence was found on the regular all-reflection map. The anharmonicity of the C7, C8, C9 and O9 atoms becomes apparent by the presence of the well known alternating positive–negative patterns around the atomic positions (Mallinson *et al.*, 1988; Scheins *et al.*, 2010; Herbst-Irmer *et al.*, 2013; Jarzembska, Kamiński *et al.*, 2014). Interestingly, all atoms seem to vibrate in a synchronous way, which indicates some anharmonic vibration of the whole uracil fragment. Fig. 8 shows the comparison of models with and without (harmonic approximation only) anharmonicity taken into account. It is clearly seen that the anharmonic corrections are not needed at 10 K, whereas they become increasingly important at higher temperatures. The 300 K map for the harmonic model seems to be a bit 'blurry' presumably due to the incomplete deconvolution of the electron density and thermal motion features (especially visible in the vicinity of the O9 atom, where the anharmonic pattern seems to be absent). Nevertheless, in all the cases (*i.e.* at 100, 200 and 300 K) the anharmonic motion was properly accounted for by refining the third-order Gram–Charlier parameters. After the refinement all high-resolution residual density features significantly diminish and become more random. Detailed examination of numerical values for anharmonic parameters (Table 5) reveals their strong dependence on temperature. The average increase of the anharmonic parameters' magnitudes when elevating temperature from 100 to 300 K is around a factor of 4 or 5, and in some cases (parameter C_{112} for the O9 atom) it reaches 7. The dependence of these two selected parameters *versus* squared temperature of the measurement (T^2) is approximately linear (Fig. 9).

Harmonic atomic displacement parameters of the whole moiety were analysed so as to better understand the more pronounced

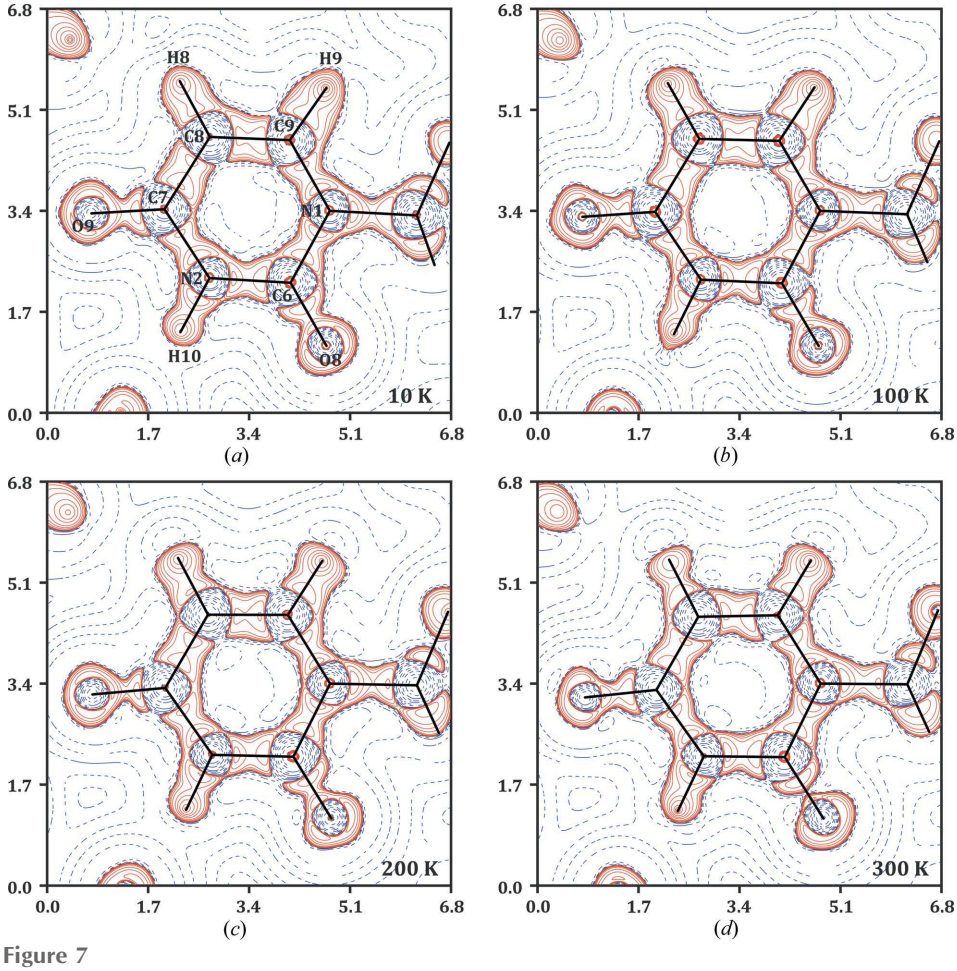

Figure 7
Laplacian maps for the uracil fragment (logarithmic contours; blue dashed lines – positive values, red solid lines – negative values). The common atom labelling is shown only in (*a*).

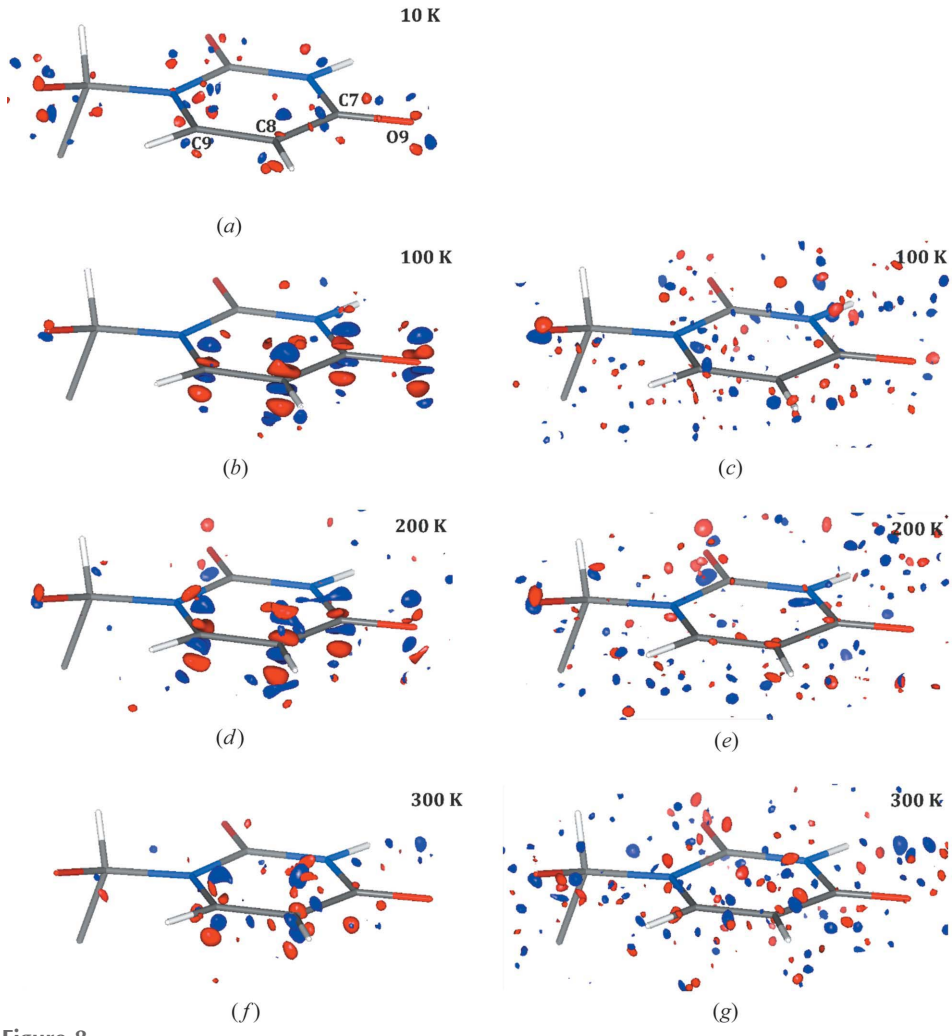

Figure 8
High-resolution ($0.8 \leq \sin\theta/\lambda \leq 1.2$ Å^{-1}) residual density isosurfaces for the uracil fragment. Left panels (*a*, *b*, *d*, *f*) – harmonic models, right panels (*c*, *e*, *g*) – models with anharmonicity introduced for the C7, C8, C9 and O9 atoms. Residual density values were computed with reflections fulfilling the $I \geq 3\sigma(I)$ condition; blue surfaces – positive values, red surfaces – negative values; isocontours: (*a*) 0.20 e Å^{-3}, (*b*, *d*) 0.15 e Å^{-3}, (*c*) 0.11 e Å^{-3}, (*e*) 0.12 e Å^{-3}, (*f*) 0.13 e Å^{-3} and (*g*) 0.10 e Å^{-3} (different isocontours are used to better illustrate the effects in each case).

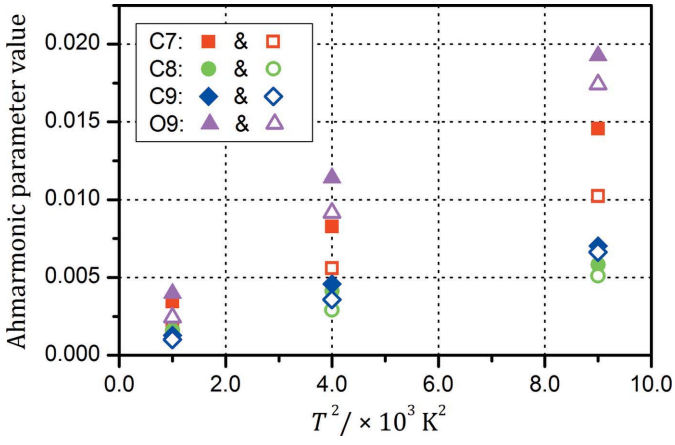

Figure 9
Dependence of the two largest anharmonic parameters (C_{111} and C_{112}) for the C7, C8, C9 and O9 atoms on squared temperature (C_{111} – solid symbols, C_{112} – open symbols).

anharmonicity for only some part of the uracil ring. These are presented in Table 6 as atomic root-square displacements along the principal axes (Waser, 1955; Busing & Levy, 1958; Sands, 1982). The largest value for each atom corresponds to the direction approximately perpendicular to the uracil ring. Whereas all values roughly linearly increase with the temperature, the largest values are observed for the atoms undergoing the anharmonic motion at elevated temperatures (*i.e.* from 100 K up). However, at 10 K both sets of values are quite comparable. The above analysis can also be represented by an increase in the displacement ellipsoids (Fig. 10) with temperature. Providing the atomic approximation to the probability density function is valid, the more restrained part of the ring, which is bound to the potassium ion through the O8 oxygen (the potassium cation is located off the uracil plane), and *additionally* involved in the relatively strong N2—H10···O2 hydrogen bond (Table 4), limits thermal vibrations of the corresponding atoms and makes them less dependent on temperature. Consequently, in that case the atoms' potential well can be satisfactorily represented by the harmonic model. In turn, the other part of the uracil ring (C7, C8 atoms and their neighbours) is bound to potassium through the O9 atom (potassium cation is located in-plane with respect to the uracil ring), and by the relatively *weak* (according to the Espinosa–Lecomte approximation around seven times weaker) and distant intramolecular C9—H9···O1 contact (Table 4). A lack of significant electrostatic forces and any additional *stronger* secondary interactions in that fragment (comparable to classical hydrogen bonds) leads to the 'freedom' of the increased atoms, thus allowing higher vibrational states to be populated, where the harmonic approximation is clearly not fulfilled. It should also be noted that the latter moiety constitutes the most weakly interacting part of the K(UMPH) molecule with its crystal surrounding.

The asymmetry of the uracil fragment neighbourhood is illustrated well in Fig. 11. In the picture the *fragment* Hirshfeld surface of uracil is surrounded by the surfaces of the potassium cations, as well as the phosphate and ribofuranose

moieties, all coloured on the basis of the respective electrostatic potential (ESP). The ESP shows that the left-hand side of the uracil ring (as oriented in Fig. 11) exhibits more complementary electrostatic interactions with its neighbours (red/blue regions – *e.g.* potassium and oxygen interactions, the N2—H10···O2 hydrogen bond) than the other part of this moiety. Indeed, the right-hand side of the uracil moiety is clearly not so strongly bound by electrostatic interactions, thus, as presumed, can undergo anharmonic motion in a more pronounced way. In view of the above, it is particularly interesting that despite the presence of the K···O9 interaction, O9 still undergoes significant anharmonic motion. Thus, the N—H···O hydrogen bond seems to be crucial for the stability/rigidity of the left part of the ring, as well as the out-of-plane interaction of the uracil O8 oxygen with the potassium ion. Otherwise, the uracil ring fragment is not involved in any significant interactions of any nature perpendicular to its plane, which could effectively restrain atomic motion along that direction (see also the supporting information).

Table 6
Root-mean-square displacement factors (given in Å) along the principal axes for uracil fragment non-H atoms.

Values are sorted from the largest to the smallest. Anharmonically modelled atoms on the left-hand side and the harmonically modelled atoms on the right-hand side.

Atom	10 K	100 K	200 K	300 K	Atom	10 K	100 K	200 K	300 K
C7	0.097	0.156	0.216	0.261	C6	0.081	0.114	0.151	0.185
	0.073	0.095	0.126	0.133		0.063	0.077	0.111	0.137
	0.064	0.083	0.109	0.156		0.060	0.085	0.100	0.125
C8	0.121	0.192	0.270	0.329	N1	0.095	0.134	0.180	0.222
	0.070	0.081	0.104	0.128		0.071	0.093	0.123	0.153
	0.068	0.094	0.123	0.152		0.062	0.085	0.110	0.135
C9	0.103	0.157	0.218	0.265	N2	0.078	0.112	0.149	0.184
	0.065	0.080	0.103	0.127		0.063	0.082	0.118	0.130
	0.068	0.087	0.113	0.140		0.068	0.089	0.107	0.145
O9	0.126	0.200	0.280	0.345	O8	0.101	0.141	0.190	0.237
	0.088	0.117	0.155	0.192		0.081	0.107	0.142	0.174
	0.065	0.082	0.109	0.136		0.063	0.082	0.108	0.131

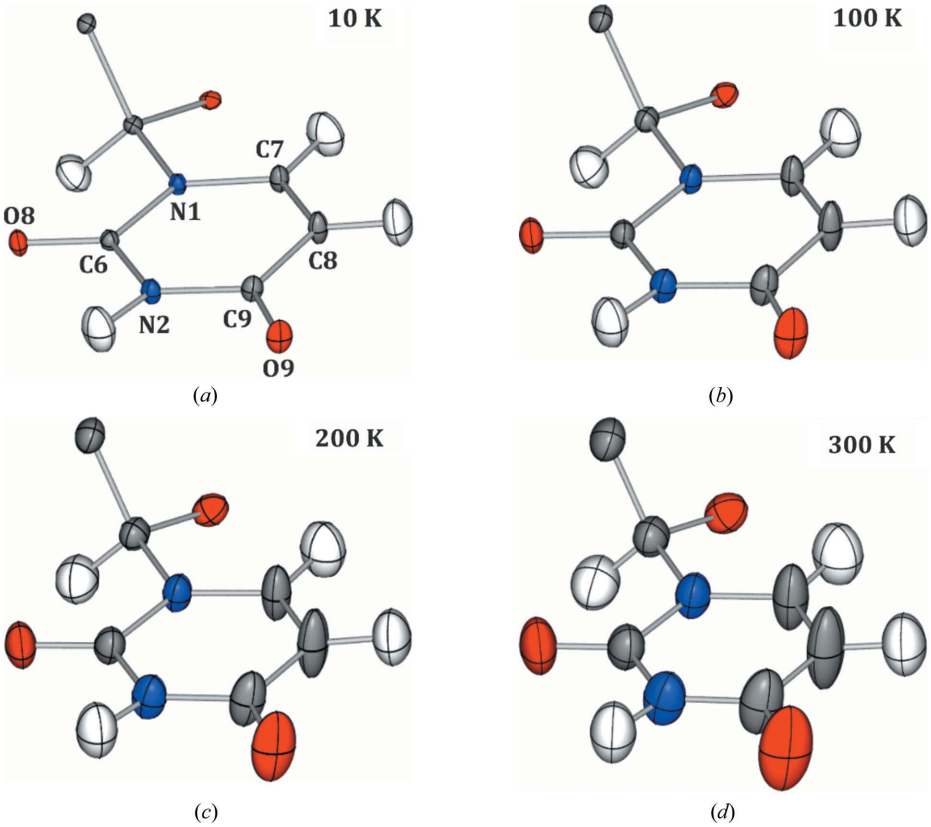

Figure 10
Anisotropic atomic displacement parameters represented as displacement ellipsoids (70% probability level) for the uracil ring at different temperatures for the final models.

4. Summary

Four high-resolution X-ray diffraction data sets at different temperatures, 10, 100, 200 and 300 K (the latter collected up to the outstanding resolution of 1.21 $Å^{-1}$ as for room-temperature measurement), were successfully collected. The studied uridine-5′-monophosphate potassium salt, K(UMPH), crystallizes in the $P2_12_12_1$ space group and forms high-quality single crystals. The ionic K(UMPH) crystal structure is naturally stabilized by predominant electrostatic forces. As shown by the generated electrostatic potential map, the complementary charged fragments are located next to another to optimize the total attractive energy and minimize the repulsive forces. Additionally, four types of hydrogen bond interactions can be found in the structure, as well as numerous weaker interatomic contacts. In contrast to the related structures deposited in the CSD, K(UMPH) does not create a layered architecture but a rather compact and more uniform structure in all dimensions, which validates the observed crystal quality.

At the multipolar refinement stage two models for the potassium ion were tested – spherical and aspherical. Periodic DFT computations supported the decision to us the spherical model in the examined case. As potassium is charged and coordinated in a relatively uniform way by seven oxygen atoms, such an outcome seems sensible. Topological analysis of the

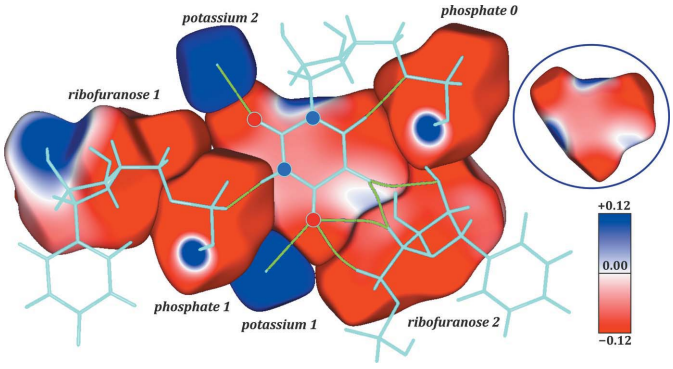

Figure 11
Fragment Hirshfeld surfaces around the uracil moiety coloured with the electrostatic potential computed on the basis of the multipole model (10 K data set; blue colour – positive values, red – negative; all values are in e Å^{-1}). Respective molecular fragments are labelled and shown as bright turquoise thick lines overlaid on the surfaces. Selected bond paths are shown in green. For the uracil moiety the N and O atoms are represented as blue and red circles, respectively. In a black circle in the upper right corner the full uracil surface is presented to show the part covered by phosphate 1 in the full picture.

electron density distribution revealed its interesting features and indicated its dependence on temperature. Multipole models for higher-temperature data sets (200 K and 300 K) are of visibly lower quality, and exhibit some problems when compared with the models obtained from the 10 K and 100 K data sets. This is most probably due to the incomplete deconvolution of thermal motion from the static electron density distribution. At 100 K and at higher temperatures we observed the well known alternated patterns in the residual density maps for some uracil ring atoms. Such features constitute usually a sign of anharmonic motion, and, indeed, were well accounted for with the Gram-Charlier parameters. Firm evidence for anharmonic motion was provided by the 10 K data set showing no residual density features of this kind. The elevated anharmonic motion observed in a fragment of the uracil ring, when compared with the remaining part of the molecule, could have resulted from its relatively weak interactions with the crystal surroundings. Otherwise, the charge density distribution of the uracil ring in K(UMPH) resembles that obtained for related literature examples.

Acknowledgements

The authors would like to thank Philip Coppens (Buffalo, NY, USA) for facilitating high-resolution X-ray diffraction data collection at 10 K in his laboratory. Jason B. Benedict (Buffalo, NY, USA) is thanked for assistance in these experiments. Assistance from Carlo Gatti (Milan, Italy) regarding the *TOPOND* program is gratefully acknowledged. Last but not least, Tadeusz Lis (Wrocław, Poland) is thanked for stimulating discussions and encouragement.

Funding information

The following funding is acknowledged: Wrocław Centre for Networking and Supercomputing (grant No. 285). The Science and Technology Facilities Council in the United Kingdom is gratefully acknowledged for access to neutron beamtime at ISIS, and also for the provision of sample preparation at the SXD instrument (proposal No. RB1120424). The Wrocław Centre for Networking and Supercomputing is thanked for providing computational facilities.

References

Allen, F. H. (2002). *Acta Cryst.* B**58**, 380–388.
Allen, F. H. & Bruno, I. J. (2010). *Acta Cryst.* B**66**, 380–386.
Allen, F. H., Kennard, O., Watson, D. G., Brammer, L., Orpen, A. G. & Taylor, R. (1987). *J. Chem. Soc. Perkin Trans. 2*, pp. S1–19.
Bader, R. F. W. (1994). *Atoms in Molecules: A Quantum Theory*. Oxford University Press.
Becke, A. D. (1988). *Phys. Rev. A*, **38**, 3098–3100.
Becker, P. J. & Coppens, P. (1974*a*). *Acta Cryst.* A**30**, 148–153.
Becker, P. J. & Coppens, P. (1975*b*). *Acta Cryst.* A**31**, 417–425.
Becker, P. J. & Coppens, P. (1975). *Acta Cryst.* A**31**, 417–425.
Bertini, L., Cargnoni, F. & Gatti, C. (2007). *Theor. Chem. Acc.* **117**, 847–884.
Bindzus, N., Straasø, T., Wahlberg, N., Becker, J., Bjerg, L., Lock, N., Dippel, A.-C. & Iversen, B. B. (2014). *Acta Cryst.* A**70**, 39–48.
Blessing, R. H. (1987). *Crystallogr. Rev.* **1**, 3–58.
Blessing, R. H. (1995). *Acta Cryst.* A**51**, 33–38.
Blessing, R. H. (1997). *J. Appl. Cryst.* **30**, 421–426.
Bruker (2015). *APEX*3. Bruker AXS Inc., Madison, Wisconsin, USA.
Busing, W. R. & Levy, H. A. (1958). *Acta Cryst.* **11**, 450–451.
Chęcińska, L., Mebs, S., Hübschle, C. B., Förster, D., Morgenroth, W. & Luger, P. (2006). *Org. Biomol. Chem.* **4**, 3242–3251.
Conole, G., Clough, A. & Whiting, A. (1995). *Acta Cryst.* C**51**, 1056–1059.
Czyżnikowska, Z., Góra, R. W., Zaleśny, R., Lipkowski, P., Jarzembska, K. N., Dominiak, P. M. & Leszczynski, J. (2010). *J. Phys. Chem. B*, **114**, 9629–9644.
Desch, M., Schinner, E., Kees, F., Hofmann, F., Seifert, R. & Schlossmann, J. (2010). *FEBS Lett.* **584**, 3979–3984.
Dominiak, P. M., Makal, A., Mallinson, P. R., Trzcinska, K., Eilmes, J., Grech, E., Chruszcz, M., Minor, W. & Woźniak, K. (2006). *Chem. Eur. J.* **12**, 1941–1949.
Dos Santos, L. H. R., Genoni, A. & Macchi, P. (2014). *Acta Cryst.* A**70**, 532–551.
Dovesi, R., Orlando, R., Civalleri, B., Roetti, C., Saunders, V. R. & Zicovich-Wilson, C. M. (2005). *Z. Kristallogr.* **220**, 571–573.
Dovesi, R., Saunders, V. R., Roetti, C., Orlando, R., Zicovich-Wilson, C. M., Pascale, F., Civalleri, B., Doll, K., Harrison, N. M., Bush, I. J., D'Arco, P. & Llunell, M. (2009). *CRYSTAL09*. Univerity of Torino, Italy.
Ekstrom, C. R., Schmiedmayer, J., Chapman, M. S., Hammond, T. D. & Pritchard, D. E. (1995). *Phys. Rev. A*, **51**, 3883–3888.
Emerson, J. & Sundaralingam, M. (1980). *Acta Cryst.* B**36**, 537–543.
Espinosa, E., Lecomte, C. & Molins, E. (1999). *Chem. Phys. Lett.* **300**, 745–748.
Espinosa, E., Lecomte, C., Molins, E., Veintemillas, S., Cousson, A. & Paulus, W. (1996). *Acta Cryst.* B**52**, 519–534.
Espinosa, E., Molins, E. & Lecomte, C. (1998). *Chem. Phys. Lett.* **285**, 170–173.
Fajardo, A. M., Piazza, G. A. & Tinsley, H. N. (2014). *Cancers*, **6**, 436–458.
Fischer, A., Tiana, D., Scherer, W., Batke, K., Eickerling, G., Svendsen, H., Bindzus, N. & Iversen, B. B. (2011). *J. Phys. Chem. A*, **115**, 13061–13071.
Gatti, C., Saunders, V. R. & Roetti, C. (1994). *J. Chem. Phys.* **101**, 10686–10696.
Grabowski, S. J. (2001). *J. Mol. Struct.* **562**, 137–143.

Groom, C. R., Bruno, I. J., Lightfoot, M. P. & Ward, S. C. (2016). *Acta Cryst.* B**72**, 171–179.
Guillot, B. (2012). *Acta Cryst.* A**68**, s204.
Guillot, B., Viry, L., Guillot, R., Lecomte, C. & Jelsch, C. (2001). *J. Appl. Cryst.* **34**, 214–223.
Hansen, N. K. & Coppens, P. (1978). *Acta Cryst.* A**34**, 909–921.
Harrison, W. T. A. & Wardell, J. L. (2014). *Acta Cryst.* E**70**, 68–71.
Herbst-Irmer, R., Henn, J., Holstein, J. J., Hübschle, C. B., Dittrich, B., Stern, D., Kratzert, D. & Stalke, D. (2013). *J. Phys. Chem. A*, **117**, 633–641.
Hibbs, D. E., Howard, S. T., Huke, J. P. & Waller, M. P. (2005). *Phys. Chem. Chem. Phys.* **7**, 1772–1778.
Hirshfeld, F. L. (1976). *Acta Cryst.* A**32**, 239–244.
Holmgren, W. F., Revelle, M. C., Lonij, V. P. A. & Cronin, A. D. (2010). *Phys. Rev. A*, **81**, 053608–053601–053607.
Hooft, R. W. W., Straver, L. H. & Spek, A. L. (2008). *J. Appl. Cryst.* **41**, 96–103.
Hoser, A. A., Dobrzycki, Ł., Gutmann, M. J. & Woźniak, K. (2010). *Cryst. Growth Des.* **10**, 5092–5104.
Hoser, A. A., Dominiak, P. M. & Woźniak, K. (2009). *Acta Cryst.* A**65**, 300–311.
Howard, S. T., Huke, J. P., Mallinson, P. R. & Frampton, C. S. (1994). *Phys. Rev. B*, **49**, 7124–7136.
Janicki, R. & Starynowicz, P. (2010). *Acta Cryst.* B**66**, 559–567.
Jarzembska, K. N. & Dominiak, P. M. (2012). *Acta Cryst.* A**68**, 139–147.
Jarzembska, K. N., Goral, A. M., Gajda, R. & Dominiak, P. M. (2013). *Cryst. Growth Des.* **13**, 239–254.
Jarzembska, K. N., Hoser, A. A., Kamiński, R., Madsen, A. Ø., Durka, K. & Woźniak, K. (2014). *Cryst. Growth Des.* **14**, 3453–3465.
Jarzembska, K. N., Kamiński, R., Dobrzycki, Ł. & Cyrański, M. K. (2014). *Acta Cryst.* B**70**, 847–855.
Jarzembska, K. N., Kamiński, R., Dobrzycki, Ł. & Cyrański, M. K. (2015). *Acta Cryst.* B**71**, 241–243.
Jarzembska, K. N., Kamiński, R., Wenger, E., Lecomte, C. & Dominiak, P. M. (2013). *J. Phys. Chem. C*, **117**, 7764–7775.
Jarzembska, K. N., Kubsik, M., Kamiński, R., Woźniak, K. & Dominiak, P. M. (2012). *Cryst. Growth Des.* **12**, 2508–2524.
Jayatilaka, D. & Grimwood, D. J. (2001). *Acta Cryst.* A**57**, 76–86.
Jelsch, C., Guillot, B., Lagoutte, A. & Lecomte, C. (2005). *J. Appl. Cryst.* **38**, 38–54.
Jelsch, C., Teeter, M. M., Lamzin, V., Pichon-Pesme, V., Blessing, R. H. & Lecomte, C. (2000). *Proc. Natl Acad. Sci. USA*, **97**, 3171–3176.
Johnson, C. K. (1969). *Acta Cryst.* A**25**, 187–194.
Jørgensen, M. R. V., Cenedese, S., Clausen, H. F., Overgaard, J., Chen, Y.-S., Gatti, C. & Iversen, B. B. (2013). *Inorg. Chem.* **52**, 297–305.
Kamiński, R., Domagała, S., Jarzembska, K. N., Hoser, A. A., Sanjuan-Szklarz, W. F., Gutmann, M. J., Makal, A., Malińska, M., Bąk, J. M. & Woźniak, K. (2014). *Acta Cryst.* A**70**, 72–91.
Kamiński, R., Jarzembska, K. N., Dąbrowski, M., Durka, K., Kubsik, M., Serwatowski, J. & Woźniak, K. (2016). *Cryst. Growth Des.* **16**, 1687–1700.
Kamiński, R., Jarzembska, K. N. & Domagała, S. (2013). *J. Appl. Cryst.* **46**, 540–543.
Keen, D. A., Gutmann, M. J. & Wilson, C. C. (2006). *J. Appl. Cryst.* **39**, 714–722.
Kinzhybalo, V., Mermer, A., Lis, T. & Starynowicz, P. (2013). *Acta Cryst.* B**69**, 344–355.
Klohs, W. D., Wilson, J. R., Weiser, M. M., Frankfurt, O. & Bernacki, R. J. (1984). *J. Cell. Physiol.* **119**, 23–28.
Koritsanszky, T., Zobel, D. & Luger, P. (2000). *J. Phys. Chem. A*, **104**, 1549–1556.
Kuhs, W. F. (1983). *Acta Cryst.* A**39**, 148–158.
Kuhs, W. F. (1988). *Aust. J. Phys.* **41**, 369–382.
Kuhs, W. F. (1992). *Acta Cryst.* A**48**, 80–98.
Lee, C., Yang, W. & Parr, R. G. (1988). *Phys. Rev. B*, **37**, 785–789.
Macchi, P. & Coppens, P. (2001). *Acta Cryst.* A**57**, 656–662.
Madsen, A. Ø. (2006). *J. Appl. Cryst.* **39**, 757–758.
Mallinson, P. R., Koritsanszky, T., Elkaim, E., Li, N. & Coppens, P. (1988). *Acta Cryst.* A**44**, 336–343.
Massa, L., Goldberg, M., Frishberg, C., Boehme, R. F., La Placa, S. J. & Lett, P. R. (1985). *Phys. Rev. Lett.* **55**, 622–625.
Meindl, K. & Henn, J. (2008). *Acta Cryst.* A**64**, 404–418.
Meindl, K., Henn, J., Kocher, N., Leusser, D., Zachariasse, K. A., Sheldrick, G. M., Koritsanszky, T. & Stalke, D. (2009). *J. Phys. Chem. A*, **113**, 9684–9691.
Mermer, A., Lis, T. & Starynowicz, P. (2015). *RSC Adv.* **5**, 96623–96638.
Mermer, A. & Starynowicz, P. (2011). *Acta Cryst.* B**67**, 399–408.
Mermer, A. & Starynowicz, P. (2012). *Acta Cryst.* B**68**, 625–635.
Molof, R. W., Schwartz, H. L., Miller, T. M. & Bederson, B. (1974). *Phys. Rev. A*, **10**, 1131–1140.
Moss, G. R., Souhassou, M., Blessing, R. H., Espinosa, E. & Lecomte, C. (1995). *Acta Cryst.* B**51**, 650–660.
Munshi, P. & Row, T. N. . (2006). *Acta Cryst.* B**62**, 612–626.
Munshi, P., Madsen, A. Ø., Spackman, M. A., Larsen, S. & Destro, R. (2008). *Acta Cryst.* A**64**, 465–475.
Nelyubina, Y. V., Troyanov, S. I., Antipin, M. Y. & Lyssenko, K. A. (2009). *J. Phys. Chem. A*, **113**, 5151–5156.
Niepötter, B., Herbst-Irmer, R. & Stalke, D. (2015). *J. Appl. Cryst.* **48**, 1485–1497.
Oszlányi, G. & Sütő, A. (2004). *Acta Cryst.* A**60**, 134–141.
Oszlányi, G. & Sütő, A. (2005). *Acta Cryst.* A**61**, 147–152.
Overgaard, J., Schiøtt, B., Larsen, F. K. & Iversen, B. B. (2001). *Chem. Eur. J.* **7**, 3756–3767.
Palatinus, L. (2013). *Acta Cryst.* B**69**, 1–16.
Palatinus, L. & Chapuis, G. (2007). *J. Appl. Cryst.* **40**, 786–790.
Paul, A., Kubicki, M., Jelsch, C., Durand, P. & Lecomte, C. (2011). *Acta Cryst.* B**67**, 365–378.
Peintinger, M. F., Oliveira, D. V. & Bredow, T. (2013). *J. Comput. Chem.* **34**, 451–459.
Perdew, J. P. (1986). *Phys. Rev. B*, **33**, 8822–8824.
Petříček, V., Dušek, M. & Palatinus, L. (2014). *Z. Kristallogr.* **229**, 345–352.
Poulain, A., Wenger, E., Durand, P., Jarzembska, K. N., Kamiński, R., Fertey, P., Kubicki, M. & Lecomte, C. (2014). *IUCrJ*, **1**, 110–118.
Poulain-Paul, A., Nassour, A., Jelsch, C., Guillot, B., Kubicki, M. & Lecomte, C. (2012). *Acta Cryst.* A**68**, 715–728.
Romano, A. H. & Conway, T. (1996). *Res. Microbiol.* **147**, 448–455.
Roversi, P. & Destro, R. (2004). *Chem. Phys. Lett.* **386**, 472–478.
Sands, D. E. (1982). *Vectors and Tensors in Crystallography*. Reading, MA: Addinson-Wesley Publishing Company.
Scheins, S., Zheng, S.-L., Benedict, J. B. & Coppens, P. (2010). *Acta Cryst.* B**66**, 366–372.
Scheringer, C. (1985). *Acta Cryst.* A**41**, 79–81.
Seshadri, T. P., Viswamitra, M. A. & Kartha, G. (1980). *Acta Cryst.* B**36**, 925–927.
Shefter, E. & Trueblood, K. N. (1965). *Acta Cryst.* **18**, 1067–1077.
Śledź, P., Kamiński, R., Chruszcz, M., Zimmerman, M. D., Minor, W. & Woźniak, K. (2010). *Acta Cryst.* B**66**, 482–492.
Sørensen, H. O. & Larsen, S. (2003). *J. Appl. Cryst.* **36**, 931–939.
Souhassou, M., Espinosa, E., Lecomte, C. & Blessing, R. H. (1995). *Acta Cryst.* B**51**, 661–668.
Spek, A. L. (2015). *Acta Cryst.* C**71**, 9–18.
Srikrishnan, T., Fridey, S. M. & Parthasarathy, R. (1979). *J. Am. Chem. Soc.* **101**, 3739–3744.
Starynowicz, P. & Lis, T. (2014). *Acta Cryst.* B**70**, 723–731.
Su, Z. & Coppens, P. (1998). *Acta Cryst.* A**54**, 646–652.
Viswamitra, M. A., Post, M. L. & Kennard, O. (1979). *Acta Cryst.* B**35**, 1089–1094.
Viswamitra, M. A., Reddy, B. S., James, M. N. G. & Williams, G. J. B. (1972). *Acta Cryst.* B**28**, 1108–1116.
Viswamitra, M. A., Seshadri, T. P. & Post, M. L. (1980). *Acta Cryst.* B**36**, 2019–2024.

Volkov, A., Li, X., Koritsanszky, T. & Coppens, P. (2004). *J. Phys. Chem. A*, **108**, 4283–4300.
Volkov, A., Macchi, P., Farrugia, L. J., Gatti, C., Mallinson, P., Richter, T. & Koritsanszky, T. (2016). *XD2016.* University at Buffalo, State University of New York, Buffalo, NY, USA, http://www.chem.gla.ac.uk/~louis/xd-home.
Wan, L., Cao, D., Zeng, J., Yan, R. & Pizzorno, G. (2006). *Mol. Pharmacol.* **69**, 1389–1395.
Wan, Y., Kertesz, M., Spitale, R. C., Segal, E. & Chang, H. Y. (2011). *Nat. Rev. Genet.* **12**, 641–655.
Waser, J. (1955). *Acta Cryst.* **8**, 731.
Wilson, C. C. (1997). *J. Appl. Cryst.* **30**, 184–189.
Wu, A. F. & Chargaff, E. (1969). *Proc. Natl Acad. Sci. USA*, **63**, 1222–1226.
Wurtman, R. J., Cansev, M., Sakamoto, T. & Ulus, I. H. (2009). *Annu. Rev. Nutr.* **29**, 59–87.
Yufit, D. S., Howard, J. A. K. & Davidson, M. G. (2000). *J. Chem. Soc. Perkin Trans. 2*, pp. 249–253.
Zarychta, B., Zaleski, J., Kyzioł, J., Daszkiewicz, Z. & Jelsch, C. (2011). *Acta Cryst.* B**67**, 250–262.
Zhurov, V. V. & Pinkerton, A. A. (2013). *Z. Anorg. Allg. Chem.* **639**, 1969–1978.
Zhurov, V. V., Zhurova, E. A., Stash, A. I. & Pinkerton, A. A. (2011). *Acta Cryst.* A**67**, 160–173.